Tb³⁺-doped borosilicate glass scintillators for high-resolution X-ray imaging

Wenjun Huang (黄文俊), Junyu Chen (陈俊宇), Yi Li (李 怡), Yueyue Wu (吴悦悦), Lianjie Li (李连杰),
Liping Chen (陈莉萍), and Hai Guo (郭 海)*

Department of Physics, Zhejiang Normal University, Jinhua 321004, China

*Corresponding author: ghh@zjnu.cn

Scintillators are the vital component in X-ray perspective image technology that is applied in medical imaging, industrial nondestructive testing, and safety testing. But the high cost and small size of single-crystal commercialized scintillators limit their practical application. Here, a series of Tb³⁺-doped borosilicate glass (BSG) scintillators with big production size, low cost, and high spatial resolution are designed and fabricated. The structural, photoluminescent, and scintillant properties are systematically investigated. Benefiting from excellent transmittance (87% at 600 nm), high interquantum efficiency (60.7%), and high X-ray excited luminescence (217% of $Bi_4Ge_3O_{12}$), the optimal sample shows superhigh spatial resolution (exceeding 20 lp/mm). This research suggests that Tb³⁺-doped BSG scintillators have potential applications in the static X-ray imaging field.

Keywords: scintillators; borosilicate glass; X-ray imaging; Tb³⁺; high spatial resolution.

1. Introduction

Scintillators can absorb high-energy rays or particles (X-ray or γ particles) and emit photons in the visible range[1–4]. They are the vital component in X-ray perspective image technology that has been applied in medical imaging, industrial nondestructive testing, safety testing, and many other fields[1–10]. At present, the commercial scintillators are mainly single-crystal scintillators with excellent scintillation performance, e.g., $CdWO_4$ (CWO), $Bi_4Ge_3O_{12}$ (BGO), CsI:Tl, and $(Lu,Y)_2SiO_5$:Ce (LYSO)[11]. However, the difficulties faced by single crystals in reducing the cost and achieving large scale and sizes production limit their further development[12–16]. Low-cost preparation of large-sized scintillators with high spatial resolution is important and urgent. Therefore, many different materials have been widely investigated in scintillating fields[17–21]. Glass scintillators stand out because of their mature process, excellent transmittance, high rare-earth ions (REIs) solubility, flexible plasticity, and low production cost[14–19,22–28].

Silicate glass has the advantages of high heat resistance, high mechanical strength, and excellent physical-chemical stability, but it also has a high melting temperature[18,19,25]. The addition of boron oxide can effectively reduce the melting temperature, and the resulting phase separation phenomenon can be solved by adding sodium oxide. The addition of alumina can form aluminum–oxygen tetrahedrons in glass and bridge the glass network, which closes the glass structure and improves performance. The addition of barium oxide can effectively introduce heavy element barium to improve the radiation resistance and absorption of X rays. Such borosilicate glass (BSG), combined with a glass network intermediate (alumina) and glass network extras (sodium oxide and barium oxide), may present good scintillating properties in the X-ray imaging field after being activated by the appropriate REI.

Among the REI, Tb³⁺ is widely used in glass scintillators as an excellent doping activator[16,29,30]. Benefiting from the stable luminescence at 542 nm that matched well with optical cameras (such as a charge-coupled device), Tb³⁺-doped glass might be applied for static X-ray perspective image technology due to the millisecond lifetime of Tb³⁺ in a glass matrix[16,24]. Nowadays, many Tb³⁺-doped glass scintillators have been reported, and some of the relative integrated intensity of X-ray-excited luminescence (XEL) (compared with that of BGO crystals) are listed in Table 1. But there are few reports on X-ray imaging and spatial resolution. The improvement of XEL intensity and spatial resolution of Tb³⁺-doped glass scintillators is therefore an area for further development.

In this work, the BSG with the addition of alumina, sodium oxide, and barium oxide were designed and fabricated as the glass host for Tb³⁺. These Tb³⁺-doped glass specimens show excellent transmittance (87% at 600 nm). The sample doped with 6% (mole fraction) Tb³⁺ exhibits optimal performance in

Table 1. Comparison of XEL Intensities of Tb^{3+}-Doped Glass Scintillators with BGO.

Sample	Ratio	Ref.
BGO	100%	[11]
B_2O_3-GeO_2-TeO_2-Gd_2O_3-Tb_2O_3	9%	[17]
B_2O_3-GeO_2-BaF_2-GdF_3-Gd_2O_3-Lu_2O_3-Tb_2O_3	27%	[29]
B_2O_3-GeO_2-Gd_2O_3-Tb_2O_3	30%	[24]
SiO_2-B_2O_3-Al_2O_3-Gd_2O_3-Tb_4O_7	40%	[31]
Al_2O_3-B_2O_3-SiO_2-Gd_2O_3-TbF_3	67%	[16]
SiO_2-BaF_2-BaO-AlF_3-Gd_2O_3-Sb_2O_3-Tb_2O_3-Ce_2O_3	83%	[25]
SiO_2-B_2O_3-Al_2O_3-CaO-Na_2O-$TbCl_3$	104%	[18]
Al_2O_3-B_2O_3-SiO_2-Na_2O-BaO-TbF_3	217%	This work

both photoluminescence (PL) and radioluminescence. The internal quantum efficiency (IQE) reaches 60.7%, its lifetime is 3.07 ms, and the integrated XEL intensity reaches 217% of BGO. More importantly, the optimal sample presents superhigh spatial resolution (exceeding 20 lp/mm). Hence, the results indicate that Tb^{3+}-doped BSG scintillators have a certain application value in the X-ray imaging field and are worthy of future research to improve their performance.

2. Experiment

2.1. Specimen preparation

Glass specimens were produced via conventional melt-quenching on the basis of a specific constituent of (mole fraction) $13Al_2O_3$-$11B_2O_3$-$46SiO_2$-$20Na_2O$-$10BaO$-$xTbF_3$ (named as G-host with $x = 0$ and G-xTb with $x = 3, 4, 5, 6, 7$). Al_2O_3 (A.R.), SiO_2 (A.R.), Na_2CO_3 (A.R.), $BaCO_3$ (99%), H_3BO_3 (G.R.), and TbF_3 (99.99%) were selected as corresponding raw materials and weighed according to composition (total mass is 20 g). The mixture power was ground for 40 min and then transferred to a corundum crucible. After melting at 1400°C in air for 1 h, the melted liquid was dumped onto the preheated copper-steel (300°C) and gently cast with another heated copper-steel to fabricate glass specimens. The cooled glass specimens were annealed at 400°C for 4 h and then were cut and polished to 2 mm for further characterizations. The BGO crystal with a thickness of 2 mm was purchased from Shanghai Institute of Ceramics, Chinese Academy of Sciences.

2.2. Sample characterization

X-ray diffraction (XRD) patterns were analyzed utilizing an X-ray apparatus (MiniFlex/600, Rigaku) with a $CuK_{\alpha1}$ radiation source. Fourier transform infrared (FT-IR) spectra of G-host and G-6Tb were performed on an FT-IR spectrometer

(NEXUS 670, Nicolet) with KBr as a diluent for tableting. Transmission spectra were obtained in an ultraviolet-visible spectrophotometer (U-3900, Hitachi). PL spectra, photoluminescence excitation (PLE) spectra, IQE, and decay curves were measured from a multifunction fluorescence spectrometer (Edinburgh FS5, Livingston). XEL spectra were obtained in an X-ray fluorescence spectrometer (OmniFluo960, Zolix). All measures were executed at room temperature.

The static X-ray imaging system includes an X-ray source, imaging objects, scintillator sample, and optical camera. A Mini-X X-ray tube (Amptek) with Ag target was selected as the X-ray source (the input voltage is maintained at 50 kV, and the input current can be adjusted in the 5–79 μA range). An X ray partially absorbed by an imaging object (such as an encapsulated chip, ballpoint pen, or standard X-ray test pattern plate) was projected onto the scintillator glass; the resulting radiative luminescence is refracted through a prism and captured and recorded by an sCMOS camera (Teledyne Photometrics) to form X-ray images.

3. Results and Discussion

3.1. Structural properties

Figure 1(a) depicts the XRD patterns of all specimens. All samples only show diffraction humps without diffraction peaks, which means that all samples are glassy. Figure 1(b) exhibits the FT-IR spectra of G-host and G-6Tb specimens. The absorption at about 467 cm^{-1} originates from the bending vibrations of Si-O-Si and Al-O-Si bonds[32,33]. The bending vibrations of B-O-B bridge oxygen bonds give rise to the absorption at about 710 cm^{-1}[33,34]. The wide band at around 992 cm^{-1} is caused by the superposition effect of the stretching vibrations of Si-O-Si, Al-O-Si, and B-O-B bonds[32–35]. The asymmetric stretching vibrations of B-O result in the absorption at 1276 and 1396 cm^{-1}[32,33,35].

Density (ρ) and effective atomic number (Z_{eff}) are fundamental and important parameters for glass scintillation, and the Z_{eff} values are estimated using the well-known empirical equation[36],

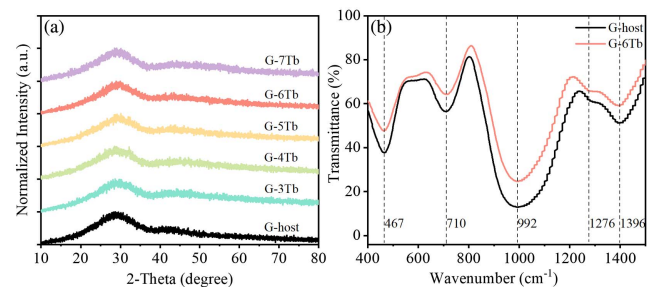$$Z_{eff} = \sqrt[2.94]{f_1(Z_1)^{2.94} + f_2(Z_2)^{2.94} + \ldots + f_i(Z_i)^{2.94}}, \quad (1)$$

Fig. 1. (a) XRD patterns of all specimens; (b) FT-IR spectra of G-host and G-6Tb specimens.

where f_i is fraction of total number of electrons associated with each element, and Z_i is the atomic number of each element. These parameters of G-xTb samples are estimated and listed in Table 2.

The transmittance of the scintillator is an important factor that affects the spatial resolution of an X-ray imaging system. The transmittance spectra of all specimens are presented in Fig. 2(a). All specimens show good transmittance, whose value is about 87%@600 nm. The absorption peaks situated at 340, 352, 368, 378, and 484 correspond to the emblematic transition of Tb^{3+} from $^7F_6$ level to $^5L_7$, $^5L_9$, and $^5D_{2,3,4}$ levels, respectively[24,29,37]. All absorption peaks become more obvious when boosting Tb^{3+} concentration. The bandgaps of G-host and G-6Tb specimens are estimated by the formula $\alpha = B(h\nu - E_g)^{1/2}$ for direct band material, where α and B mean the absorption coefficient and a constant coefficient, respectively[22], $h\nu$ is photon energy, and E_g stands for bandgap. α can be obtained by converting transmittance data through $I = I_0 e^{-ad}$ and $T = I/I_0$, where I, I_0, d, and T mean incident intensity, transmitted intensity, thickness, and transmittance, respectively. And as presented in Fig. 2(b), E_g values of G-host and G-6Tb specimens are 3.90 and 3.86 eV, respectively.

The photographs of all samples are displayed in Fig. 3. In the sunlight, all samples appear very transparent. The high transparency of samples allows the printed font to be clearly seen through the sample. And under the excitation of 365 nm light,
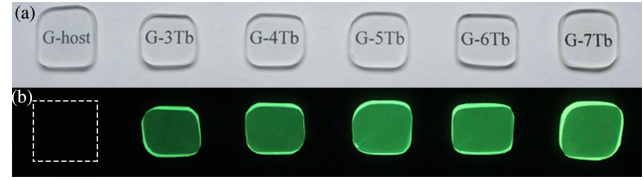
Table 2. The Density (ρ), Effective Atomic Number (Z_{eff}), IQE Values, Average Lifetime (τ) of $^5D_4$ State of Tb^{3+} (λ_{ex} = 378 nm), and the XEL Intensity (Compared to Commercial BGO Crystal) of G-xTb Specimens.

Specimen	G-3Tb	G-4Tb	G-5Tb	G-6Tb	G-7Tb
ρ	2.96	3.00	3.03	3.07	3.11
Z_{eff}	33.8	34.8	35.7	36.5	37.2
IQE (λ_{ex} = 378 nm)	45.0%	71.5%	72.5%	60.7%	59.4%
τ (ms)	3.52	3.34	3.13	3.07	3.03
XEL intensity	92%	150%	167%	217%	166%

Fig. 3. Photos of all samples (a) under daylight and (b) under 365 nm light irradiation.

G-xTb specimens present typical green emission of Tb^{3+}, whereas the G-host sample dose not emit light (labeled in white dashed box). Among G-xTb samples, G-6Tb and G-7Tb show intense green emission.

3.2. Photoluminescent properties

Figure 4(a) demonstrates the PL spectra (λ_{ex} = 378 nm) of all specimens. The PL spectra comprise peaks at 487, 542, 583, and 621 nm, which are referred to as $^5D_4$ to $^7F_{6,5,4,3}$ transition of Tb^{3+}[38–40]. By boosting Tb^{3+} contents, the emission intensities of these peaks are strengthened and then weakened. The PLE spectra (λ_{em} = 542 nm) of all samples are shown in Fig. 4(b)[23,41]. The excitation band (225–297 nm) is related to 4f^8 to 4f^{7}5d^1 electron transition (f–d) of Tb^{3+}[16,25]. These excitation peaks at 302, 316, 339, 351, 369, 378, and 484 correspond to $^7F_6$ to $^5H_{6,7}$, $^5L_{7,9}$, and $^5D_{2,3,4}$ transition of Tb^{3+}, respectively, which are consistent with Fig. 2(b)[13,25]. PL spectra and PLE spectra show that the optimal sample is the G-6Tb sample.

IQE values of the G-xTb specimens were gauged and calculated, as demonstrated in Fig. 5(a). The values of IQE enumerated in Table 2 can be computed by utilizing the following formula[41,42]:

$$\text{IQE} = \frac{\int L_{sample}}{\int E_{reference} - \int E_{sample}}, \qquad (2)$$

where L_{sample} stands for the emission intensity of sample, and $E_{reference}$ and E_{sample} mean the excitation intensity when a standard whiteboard or sample is used, respectively. G-5Tb shows the highest IQE value, which reaches 72.5%, and the G-6Tb sample also has a relatively high IQE value (60.7%). The relatively
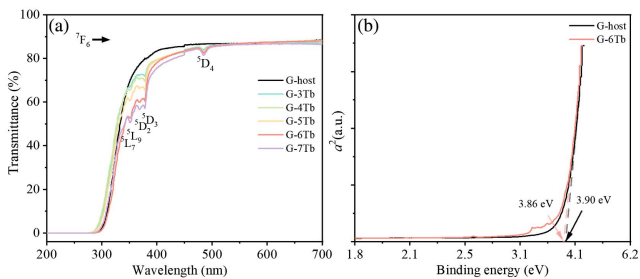

Fig. 2. (a) Transmittance spectra of all samples; (b) relationship between α^2 and $h\nu$ for G-host and G-6Tb samples.
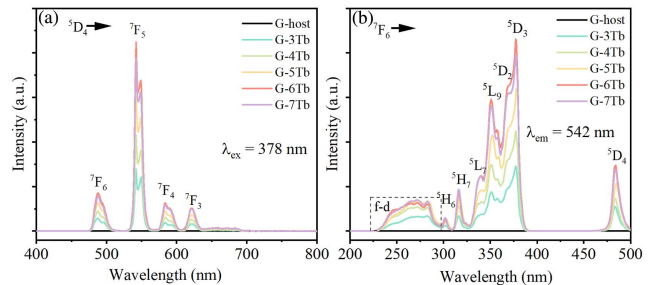

Fig. 4. (a) PL spectra (λ_{ex} = 378 nm) of all samples; (b) PLE spectra (λ_{em} = 542 nm) of all samples.
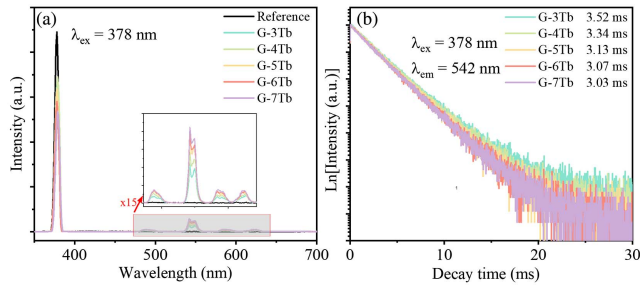
Fig. 5. (a) IQE spectra of G-xTb specimens; (b) decay curves (λ_{ex} = 378 nm) of 542 nm emission of G-xTb specimens.

high IQE might be helpful to get high XEL intensity for X-ray imaging.

The luminescence decay curves (λ_{ex} = 378 nm) of 542 nm emission of G-xTb specimens are revealed in Fig. 5(b). The τ values of $^5D_4$ state of Tb^{3+} in G-xTb specimens are calculated via the following formula[16,43]:

$$\tau = \int tI(t)\mathrm{d}t / \int I(t)\mathrm{d}t, \qquad (3)$$

where $I(t)$ is the luminescence intensity at moment t. As listed in Table 2, the τ values decrease continuously (from 3.52 to
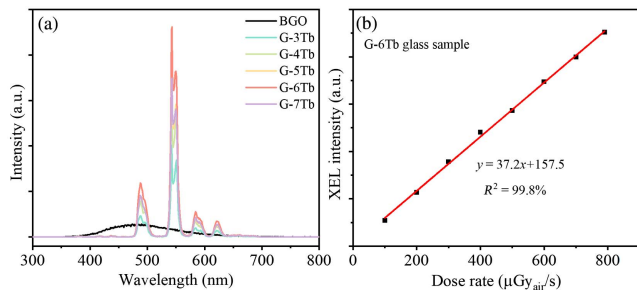

Fig. 6. (a) XEL spectra of BGO crystal and G-xTb specimens; (b) relationship between XEL intensity and X-ray dose rate.

2.98 ms) with the boost of Tb^{3+} concentration. The millisecond lifetimes of glass specimens are suitable for static X-ray imaging.

3.3. Radioluminescent properties and X-ray imaging

To characterize the scintillating capability of G-xTb specimens in X-ray imaging, Fig. 6(a) shows the XEL spectra of commercial BGO crystal and G-xTb specimens. As the Tb^{3+} concentration increases, the XEL intensity of G-xTb samples enhances gradually, and abates afterwards. The G-6Tb sample presents the optimal scintillating performance.

The ratio of the integrated XEL intensity between G-xTb samples and BGO is calculated and listed in Table 2. Notably, the XEL intensity of the G-6Tb specimen reaches 217% of that of BGO. It suggests that the G-6Tb sample might have a potential application in X-ray imaging. The relationship between XEL intensity and the X-ray dose rate of the G-6Tb sample is displayed in Fig. 6(b). These experimental data points match well (R^2 = 99.8%) with the fit line ($y = 37.2x + 157.5$), indicating that the radioluminescent intensity is critically dependent on the X-ray dose (which will create a high contrast in the X-ray imaging), suggesting their practical application[44,45].

The X-ray imaging capacity was investigated by a suborbicular G-6Tb optimal sample with $\Phi 35$ mm × 0.5 mm size and is presented in Fig. 7. The photo and X-ray-excited image of the G-6Tb specimen are displayed in Figs. 7(a) and 7(b). The homogeneity of the big glass samples can be obtained by stirring processing during the melting process. Figures 7(d) and 7(f) exhibit the X-ray images of the encapsulated chip and the ballpoint pen, and corresponding images are presented in Figs. 7(c) and 7(e). The covered content (such as wires, spring, and even ballpen ink) can be clearly observed.

The spatial resolution is one of the most important parameters for X-ray imaging. It can be obtained in the image of a standard X-ray test pattern plate [photo in Fig. 7(g)], shown in Fig. 7(h). The image distinctly shows that six light lines can be resolved, even at densities over 20 lp/mm, indicating that the optimal sample presents superhigh spatial resolution (exceeding 20 lp/mm). Such high spatial resolution can meet the
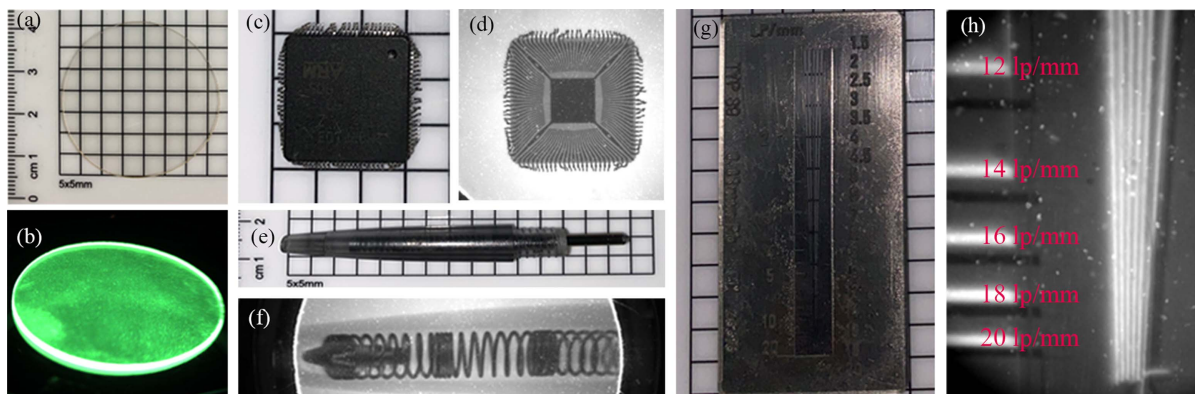

Fig. 7. Photos of G-6Tb sample for (a) X-ray imaging, (c) encapsulated chip, (e) ballpoint pen, and (g) standard X-ray test pattern plate; X-ray images of (b) sample, (d) encapsulated chip, (f) ballpoint pen, and (h) standard X-ray test pattern plate.

requirements of actual X-ray imaging. For a better comparison, the spatial resolution values of some different scintillating materials for X-ray imaging are listed in Table 3. The spatial resolution of the G-6Tb sample reaches the highest level. In brief, Tb^{3+}-doped BSG scintillators with big production size, low cost, and high spatial resolution might have latent applications in the field of X-ray detection and X-ray imaging.

Figure 8 illustrates the mechanism of Tb^{3+}-doped BSG scintillators. The conversion process happens first. The heavy atoms in glass generate a great number of high-energy particles (electrons and holes) after interacting with the X ray (photoelectric effect and Compton effect)[46]. These particles are then thermalized to produce more secondary electrons and holes[2,47]. During the subsequent transport process, the secondary electrons and holes are transported to Tb^{3+} ions in glass and pump these activator ions to higher excited levels. And in the final luminescence process, these excited Tb^{3+} ions make radioluminescence similar to PL. These pumped Tb^{3+} ions relax to $^5D_4$ level from various higher energy levels, and then jump to $^7F_{6,5,4,3}$ levels with corresponding emission light[5,16].

In the measurement of XEL spectra, the color of the G-6Tb sample changes from colorless to slightly yellow, indicating that X-ray irradiation will cause damage to glass. Figure 9(a) shows the transmittance spectra of the G-6Tb sample irradiated by an X ray with different input powers for 5 min. It is clear that the transparency at 320–550 nm decreases with the increase of input power. For a better comparison and to explain the color change mechanism, the transmittance spectra of the G-6Tb sample before irradiation, after X-ray irradiation (10 W), and their difference are displayed in Fig. 9(b). A broad absorption band at around 320–550 nm is observed, which can corresponde to the charge change absorption of Tb^{4+} ions[19,50]. Tb^{4+} ions are probably generated by the ionization of one electron of Tb^{3+} ions with the irradiation of high-energy X rays.
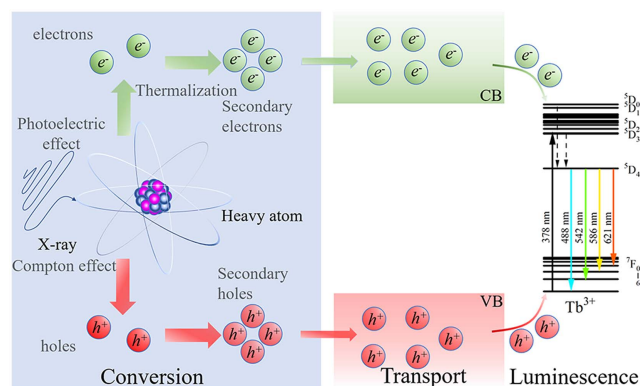

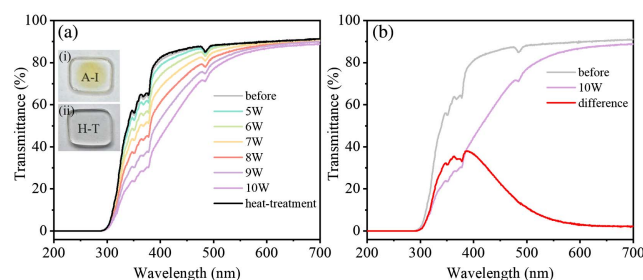**Fig. 8.** Mechanism of Tb^{3+}-doped BSG scintillators.

Fig. 9. (a) Transmittance spectra of G-6Tb sample before radiation, after being irradiated by X rays with different input powers for 5 min, and after subsequent heat treatment; inset (i) is photo of G-6Tb sample after X-ray irradiation (10 W, A-I) and inset (ii) is photo of G-6Tb sample after subsequent heat treatment (H-T); (b) transmittance spectra of G-6Tb sample before irradiation, after X-ray irradiation (10 W), and their difference.

Inset (i) is the photo of the G-6Tb specimen after 10 W of X-ray irradiation. Inset (ii) displays the photograph of the G-6Tb specimen after subsequent heat treatment (300°C for 3 h). Combined with the transmittance curve after heat treatment in Fig. 9(a), it is interesting to note that the slightly yellow absorption from Tb^{4+} ions can be restored through heat treatment.

The effect of irradiation time on XEL intensity was investigated. The XEL spectra and relative intensity curve of the G-6Tb specimen with continuous long-time X-ray irradiation (7 W) are shown in Figs. 10(a) and 10(b). With increasing irradiation time, the G-6Tb sample exhibits good irradiation luminescence stability. Only slight changes occur. The corresponding transmittance spectra of the G-6Tb sample before irradiation, after 100 min of X-ray irradiation, and their difference are displayed in Fig. 10(c). Similar to Fig. 9(c), their difference curves also exhibit absorption bands from Tb^{4+}. So, the XEL intensity changes from 100% to 94% after 100 min of X-ray irradiation, which might be the result of the absorption of Tb^{4+} produced by X-ray irradiation. The recoverable transparency by heat treatment and the good irradiation stability indicate that the G-6Tb sample might be used for X-ray imaging.

Table 3. Spatial Resolution of Diverse Material.

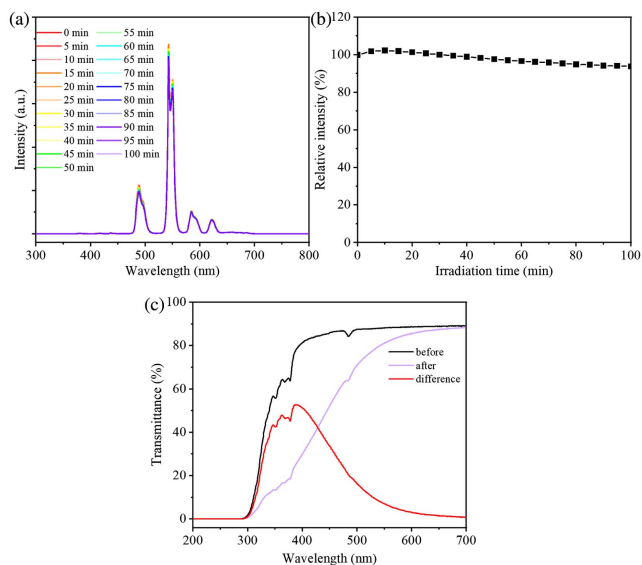| Spatial Resolution (lp/mm)	Material	Ref.
5	Mn-based halides	[48]
7.5	$CsCu_2I_3$ film	[6]
9	Cs_2ZnBr_4:Cu film	[7]
10	SiO_2-AlF_3-Al_2O_3-Gd_2O_3-Sb_2O_3-CeO_2-Tb_4O_7 glass	[49]
12.5	polymer-ceramics	[8]
15	$CsPbX_3$ nanocrystals	[9]
20	$Cs_4Mn_{0.25}Cd_{0.75}Bi_2Cl_{12}$ nanoparticles	[45]
20	Tb^{3+}-doped Ba_2LaF_7 glass ceramics	[10]
20	Al_2O_3-B_2O_3-SiO_2-Na_2O-BaO-TbF_3 glass	This work

Fig. 10. (a) XEL spectra of G-6Tb specimen with different X-ray irradiation time (7 W); (b) relative XEL intensity of G-6Tb sample after different irradiation time; (c) transmittance spectra of G-6Tb sample before irradiation, after 100 min X-ray irradiation, and their difference.

4. Conclusions

A battery of highly transparent BSG scintillators for X-ray imaging were devised and manufactured by melt-quenching technology. The transmittance of all specimens is about 87% at 600 nm, and the E_g values of samples are about 3.9 eV. The optimal G-6Tb sample presents a high IQE value (60.7%), high XEL intensity (217% of that of BGO), excellent spatial resolution (20 lp/mm), and good radiation tolerance and refreshable ability by heat treatment. The results suggest that Tb^{3+}-doped BSG scintillators with big production size, low cost, and high spatial resolution might have value for further optimization and applications in X-ray detection and X-ray imaging fields.

Acknowledgement

References

1. C. Roques-Carmes, N. Rivera, A. Ghorashi, S. E. Kooi, Y. Yang, Z. Lin, J. Beroz, A. Massuda, J. Sloan, N. Romeo, Y. Yu, J. D. Joannopoulos, I. Kaminer, S. G. Johnson, and M. Soljačić, "A framework for scintillation in nanophotonics," Science **375**, eabm9293 (2022).
2. Q. Chen, J. Wu, X. Ou, B. Huang, J. Almutlaq, A. A. Zhumekenov, X. Guan, S. Han, L. Liang, Z. Yi, J. Li, X. Xie, Y. Wang, Y. Li, D. Fan, D. B. L. Teh, A. H. All, O. F. Mohammed, O. M. Bakr, T. Wu, M. Bettinelli, H. Yang, W. Huang, and X. Liu, "All-inorganic perovskite nanocrystal scintillators," Nature **561**, 88 (2018).
3. Y. C. Kim, K. H. Kim, D. Y. Son, D. N. Jeong, J. Y. Seo, Y. S. Choi, I. T. Han, S. Y. Lee, and N. G. Park, "Printable organometallic perovskite enables large-area, low-dose X-ray imaging," Nature **550**, 87 (2017).
4. X. Ou, X. Qin, B. Huang, J. Zan, Q. Wu, Z. Hong, L. Xie, H. Bian, Z. Yi, X. Chen, Y. Wu, X. Song, J. Li, Q. Chen, H. Yang, and X. Liu, "High-resolution X-ray luminescence extension imaging," Nature **590**, 410 (2021).
5. X. Zhong, X. Wang, G. Zhan, Y. Tang, Y. Yao, Z. Dong, L. Hou, H. Zhao, S. Zeng, J. Hu, L. Cheng, and X. Yang, "NaCeF4:Gd,Tb scintillator as an X-ray responsive photosensitizer for multimodal imaging-guided synchronous radio/radiodynamic therapy," Nano Lett. **19**, 8234 (2019).
6. M. Zhang, J. Zhu, B. Yang, G. Niu, H. Wu, X. Zhao, L. Yin, T. Jin, X. Liang, and J. Tang, "Oriented-structured CsCu2I3 film by close-space sublimation and nanoscale seed screening for high-resolution X-ray imaging," Nano Lett. **21**, 1392 (2021).
7. Y. Zhou, Q. Zhou, X. Niu, Z. Yan, T. Lin, J. Xiao, and X. Han, "Compositional engineering of doped zero-dimensional zinc halide blue emitters for efficient X-ray scintillation," Inorg. Chem. Front. **9**, 2987 (2022).
8. W. Chen, M. Zhou, Y. Liu, X. Yu, C. Pi, Z. Yang, H. Zhang, Z. Liu, T. Wang, J. Qiu, S. F. Yu, Y. Yang, and X. Xu, "All-inorganic perovskite polymer–ceramics for flexible and refreshable X-ray imaging," Adv. Funct. Mater. **32**, 2107424 (2022).
9. W. Ma, T. Jiang, Z. Yang, H. Zhang, Y. Su, Z. Chen, X. Chen, Y. Ma, W. Zhu, X. Yu, H. Zhu, J. Qiu, X. Liu, X. Xu, and Y. Yang, "Highly resolved and robust dynamic X-ray imaging using perovskite glass-ceramic scintillator with reduced light scattering," Adv. Sci. **8**, 2003728 (2021).
10. H. Tang, S. Liu, Z. Fang, Z. Yang, Z. Cui, H. Lv, P. Zhang, D. Wang, F. Zhao, J. Qiu, X. Yu, and X. Xu, "High-resolution X-ray time-lapse imaging from fluoride nanocrystals embedded in glass matrix," Adv. Opt. Mater. **10**, 2102836 (2022).
11. A. Yoneyama, R. Baba, and M. Kawamoto, "Quantitative analysis of the physical properties of CsI, GAGG, LuAG, CWO, YAG, BGO, and GOS scintillators using 10-, 20- and 34-keV monochromated synchrotron radiation," Opt. Mater. Express **11**, 398 (2021).
12. R. F. Tian, M. Y. Pan, L. Zhang, and H. J. Qi, "Crystal growth and spectral properties of $(Yb_{0.15}Lu_{0.85x}Y_{0.85-0.85x})_3Al_5O_{12}$ single crystals," Chin. Opt. Lett. **20**, 121601 (2022).
13. W. Chen, J. Cao, F. Hu, R. Wei, L. Chen, X. Sun, and H. Guo, "Highly efficient Na5Gd9F32:Tb^{3+} glass ceramic as nanocomposite scintillator for X-ray imaging," Opt. Mater. Express **8**, 41 (2018).
14. S. Chen, Z. Wen, X. Peng, G. A. Ashraf, R. Wei, T. Pang, and H. Guo, "Transparent heavily Eu^{3+}-doped boroaluminate glass for X-ray detection," Ceram. Int. **48**, 947 (2022).
15. S. Y. Z. Chen, Y. J. Gong, W. J. Huang, Z. X. Wen, L. J. Li, G. A. Ashraf, L. Lei, J. K. Cao, and H. Guo, "Intense broadband radioluminescence from an Mn^{2+}-doped aluminoborate glass scintillator," J. Mater. Chem. C **10**, 10382 (2022).
16. W. Huang, Z. Wen, L. Li, G. A. Ashraf, L. Chen, L. Lei, H. Guo, and X. Li, "Photoluminescence and X-ray excited scintillating properties of Tb^{3+}-doped borosilicate aluminate glass scintillators," Ceram. Int. **48**, 17178 (2022).
17. T. Han, X. Sun, X. Lai, J. Yu, L. Xia, H. Guo, and X. Ye, "Role of Gd2O3 on tailoring structural and optical properties of Tb^{3+}-activated borogermanate-tellurite glasses," Radiat. Phys. Chem. **189**, 109734 (2021).
18. W. Chewpraditkul, Y. Shen, D. Chen, A. Beitlerova, and M. Nikl, "Luminescence of Tb^{3+}-doped high silica glass under UV and X-ray excitation," Opt. Mater. **35**, 426 (2013).
19. M. Gu, X. Jin, S. Huang, X. Liu, B. Liu, and C. Ni, "The effects of GeO2 adulterant on the luminescence properties of Tb-doped silicate glasses," Opt. Mater. **32**, 1022 (2010).
20. K. Han, K. Sakhatskyi, J. Jin, Q. Y. Zhang, M. V. Kovalenko, and Z. G. Xia, "Seed-crystal-induced cold sintering toward metal halide transparent ceramic scintillators," Adv. Mater. **34**, 2110420 (2022).
21. B. H. Li, Y. Xu, X. L. Zhang, K. Han, J. C. Jin, and Z. G. Xia, "Zero-dimensional luminescent metal halide hybrids enabling bulk transparent medium as large-area X-ray scintillators," Adv. Opt. Mater. **10**, 2102793 (2022).
22. X. Y. Liu, H. Guo, Y. Liu, S. Ye, M. Y. Peng, and Q. Y. Zhang, "Thermal quenching and energy transfer in novel Bi^{3+}/Mn^{2+} co-doped white-emitting borosilicate glasses for UV LEDs," J. Mater. Chem. C **4**, 2506 (2016).
23. C. Struebing, G. Lee, B. Wagner, and Z. T. Kang, "Synthesis and luminescence properties of Tb doped LaBGeO5 and GdBGeO5 glass scintillators," J. Alloys Compd. **686**, 9 (2016).

24. X. Sun, X. Yu, W. Wang, Y. Li, Z. Zhang, and J. Zhao, "Luminescent properties of Tb^{3+}-activated B_2O_3–GeO_2–Gd_2O_3 scintillating glasses," J. Non-Cryst. Solids **379**, 127 (2013).

25. Y. Zhang, N. Ding, T. Zheng, S. Jiang, B. Han, and J. Lv, "Effects of Ce^{3+} sensitizer on the luminescent properties of Tb^{3+}-activated silicate oxyfluoride scintillating glass under UV and X-ray excitation," J. Non-Cryst. Solids **441**, 74 (2016).

26. D. Y. Shen, J. Qian, C. W. Wang, G. D. Wang, X. H. Wang, and Q. Z. Zhao, "Facile preparation of silver nanoparticles in bulk silicate glass by high-repetition-rate picosecond laser pulses," Chin. Opt. Lett. **19**, 011901 (2021).

27. Y. G. Chen, Z. Q. Lin, Y. F. Wang, M. Wang, L. Zhang, Y. Jiao, H. H. Dong, S. K. Wang, C. L. Yu, and L. L. Hu, "Nd^{3+}-doped silica glass and fiber prepared by modified sol-gel method," Chin. Opt. Lett. **20**, 091601 (2022).

28. Y. Y. Wang, L. J. Zhong, Z. Chen, D. Z. Tan, Z. J. Fang, Y. Yang, S. Z. Sun, L. Y. Yang, and J. R. Qiu, "Photonic lattice-like waveguides in glass directly written by femtosecond laser for on-chip mode conversion," Chin. Opt. Lett. **20**, 031406 (2022).

29. X. Sun, Q. Yang, P. Gao, H. Wu, and P. Xie, "Luminescence, energy transfer properties of Tb^{3+}/Gd^{3+}-coactivated oxyfluoride borogermanate scintillating glasses," J. Lumin. **165**, 40 (2015).

30. Y. Q. Xie, Y. Jing, L. Y. Niu, C. Wang, L. Zhao, J. Ren, and J. Z. Zhang, "Perovskite-quantum-dots activated silica fiber X-ray dosimeter," Chin. Opt. Lett. **20**, 063401 (2022).

31. W. Chewpraditkul, Q. Sheng, D. Chen, A. Beitlerova, and M. Nikl, "Luminescence of Tb^{3+}-doped oxide glasses with high Gd_2O_3 concentration under UV and X-ray excitation," Phys. Status Solidi A **209**, 2578 (2012).

32. Z. Pu, J. Huang, J. Li, H. Feng, X. Wang, and X. Yin, "Effect of F content on the structure, viscosity and dielectric properties of SiO_2-Al_2O_3-B_2O_3-RO-TiO_2 glasses," J. Non-Cryst. Solids **563**, 120817 (2021).

33. Y. B. Saddeek, M. S. Gaafar, and S. A. Bashier, "Structural influence of PbO by means of FTIR and acoustics on calcium alumino-borosilicate glass system," J. Non-Cryst. Solids **356**, 1089 (2010).

34. H. Gui, C. Li, C. Lin, Q. Zhang, Z. Luo, L. Han, J. Liu, T. Liu, and A. Lu, "Glass forming, crystallization, and physical properties of MgO-Al_2O_3-SiO_2-B_2O_3 glass-ceramics modified by ZnO replacing MgO," J. Eur. Ceram. Soc. **39**, 1397 (2019).

35. H. Zhu, F. Wang, Q. Liao, D. Liu, and Y. Zhu, "Structure features, crystallization kinetics and water resistance of borosilicate glasses doped with CeO_2," J. Eur. Ceram. Soc. **518**, 57 (2019).

36. M. P. Singh, B. S. Sandhu, and B. Singh, "Measurement of effective atomic number of composite materials using scattering of γ-rays," Nucl. Instrum. Meth. A **580**, 50 (2007).

37. X. Sun, M. Zhou, C. Deng, Q. Yang, and J. Zhong, "Glass forming regions and concentration-dependent luminescence properties of Tb^{3+}-activated tellurium-lutetium-tungsten glasses," J. Rare Earths **39**, 146 (2021).

38. J. Xie, L. Cheng, H. Tang, Z. Wang, H. Sun, L. Lu, X. Mi, Q. Liu, and X. Zhang, "Wide range color tunability and efficient energy transfer of novel $NaCaGd(WO_4)_3$:Tb^{3+},Eu^{3+} phosphors with excellent thermal stability for pc-WLEDs," Inorg. Chem. Front. **8**, 4517 (2021).

39. D. A. Hakeem, J. W. Pi, S. W. Kim, and K. Park, "New $Y_2LuCaAl_2SiO_{12}$:Ln (Ln = Ce^{3+}, Eu^{3+}, and Tb^{3+}) phosphors for white LED applications," Inorg. Chem. Front. **5**, 1336 (2018).

40. J. Wang, X. Peng, D. Cheng, Z. Zheng, and H. Guo, "Tunable luminescence and energy transfer in $Y_2BaAl_4SiO_{12}$:Tb^{3+},Eu^{3+} phosphors for solid-state lighting," J. Rare Earths **39**, 284 (2021).

41. S. Y. Z. Chen, W. N. Zhang, L. M. Teng, J. Chen, X. Y. Sun, H. Guo, and X. S. Qiao, "Design, simulation, elaboration and luminescence of Tb^{3+}-doped Ba0.84Gd0.16F2.16 fluoroaluminosilicate scintillating glass ceramics," J. Eur. Ceram. Soc. **41**, 6722 (2021).

42. S. Y. Z. Chen, L. J. Li, J. Y. Chen, S. J. Xu, W. J. Huang, Z. X. Wen, T. M. Jiang, and H. Guo, "Highly resolved and refreshable X-ray imaging from Tb^{3+} doped aluminosilicate oxyfluoride glass scintillators," J. Mater. Chem. C **11**, 2389 (2023).

43. Z. X. Wen, L. J. Li, W. J. Huang, S. Y. Z. Chen, L. Lei, T. Pang, and H. Guo, "Effect of Al powder on Tb^{3+}-doped borogermanate glass for X-ray detection," J. Lumin. **250**, 119095 (2022).

44. F. Zhang, Y. Zhou, Z. Chen, M. Wang, Z. Ma, X. Chen, M. Jia, D. Wu, J. Xiao, X. Li, Y. Zhang, Z. Shi, and C. Shan, "Thermally activated delayed fluorescence zirconium-based perovskites for large-area and ultraflexible X-ray scintillator screens," Adv. Mater. **34**, 2204801 (2022).

45. C. Wang, J. Xiao, Z. Yan, X. Niu, T. Lin, Y. Zhou, J. Li, and X. Han, "Colloidal synthesis and phase transformation of all-inorganic bismuth halide perovskite nanoplates," Nano Res. **16**, 1703 (2022).

46. W. J. Huang, Y. Li, J. Y. Chen, Y. F. Zhao, L. P. Chen, and H. Guo, "Scintillating properties of gallogermanate glass scintillators doped with Tb^{3+}/Eu^{3+}," Ceram. Int. **49**, 8863 (2023).

47. C. Wang, H. Lin, Z. Zhang, Z. Qiu, H. Yang, Y. Cheng, J. Xu, X. Xiang, L. Zhang, and Y. Wang, "X-ray excited $CsPb(Cl,Br)_3$ perovskite quantum dots-glass composite with long-lifetime," J. Eur. Ceram. Soc. **40**, 2234 (2020).

48. T. Jiang, W. Ma, H. Zhang, Y. Tian, G. Lin, W. Xiao, X. Yu, J. Qiu, X. Xu, Y. Yang, and D. Ju, "Highly efficient and tunable emission of lead-free manganese halides toward white light-emitting diode and X-ray scintillation applications," Adv. Funct. Mater. **31**, 2009973 (2021).

49. Y. Wu, D. Chen, Y. Li, L. Xu, S. Wang, and S. Wu, "Scintillation properties of Ce^{3+}/Tb^{3+} co-doped oxyfluoride aluminosilicate glass for exploration of X-ray imaging," J. Lumin. **245**, 118762 (2022).

50. H. Dachraoui, R. A. Rupp, K. Lengyel, M. A. Ellabban, M. Fally, G. Corradi, L. Kovács, and L. Ackermann, "Photochromism of doped terbium gallium garnet," Phys. Rev. B **74**, 144104 (2006).